Light Manipulation and Applications
https://doi.org/10.70401/lma.2026.0003

Supplementary information

Non-Hermitian twisted photonic lattices

Jinpeng Yuan, Fuqiang Niu, Hengfei Zhang, Chaohua Wu, Gang Chen, Lirong Wang, Liantuan Xiao, Suotang Jia

S1. Energy distributions in momentum and real space

Figure S1(A) shows the momentum-space field distribution collected by the CCD with $\theta = 90°$. The beam at the top-right corner marked by *M* corresponds to the incident signal beam, while the four beams marked by *X* represent the pump and control beams. The real-space field distribution is shown in Figure S1(B), where all beams converge at a common region and undergo interference and superposition. Consequently, all beams are incident at small angles, defined as the angles between their propagation directions and the *z*-axis. According to $d = \lambda_{c,p} / 2\sin(\varphi_{c,p})$ (with $d \approx 200$ μm being the spatial period of the stripe fields) and the corresponding geometric relations, the incident angles of the pump and control beams are $\varphi_p \approx \varphi_c \approx 0.11°$, while the signal beam is incident at $\varphi_s \approx 0.15°$ in $\theta = 90°$. Although the incidence angle varies with the twisting angle, taking into account experimental alignment errors and the fault tolerance associated with the flat-band width, the signal-beam incidence angle is consistently maintained at approximately 0.15° throughout the experiments.

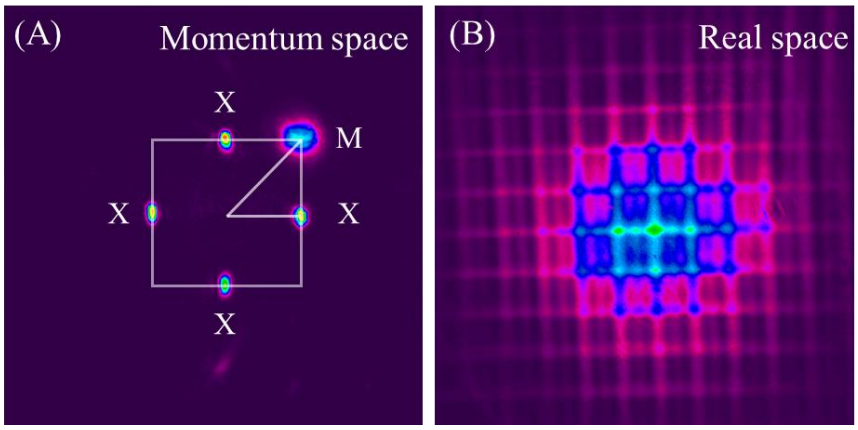

Figure S1. The experimentally measured energy distribution in (A) momentum and (B) real space of signal (at *M* points in *k* space), pump and control beams (at *X* points in *k* space).

S2. Theoretical model and refractive index calculation in a four-level *N*-type system

The control and pump fields are written as

$$\left|\tilde{\Omega}_c\right|^2 = \left|\Omega_c exp(ik_0\vec{b}_1\cdot\vec{r}) + \Omega_c exp(ik_0\vec{b}_2\cdot\vec{r})\right|^2 \quad \text{(S1)}$$

$$\left|\tilde{\Omega}_p\right|^2 = \left|\Omega_p exp(ik_0\vec{b}_3\cdot\vec{r}) + \Omega_p exp(ik_0\vec{b}_4\cdot\vec{r})\right|^2 \quad \text{(S2)}$$

where $\Omega_c=\mu_{23}E_c/\hbar$, $\Omega_p=\mu_{14}E_p/\hbar$, and $\Omega_s=\mu_{13}E_s/\hbar$ represent the Rabi frequencies of the control, pump and signal beams, μ_{ij} is the dipole momentum between levels $|i\rangle$ and $|j\rangle$, $\vec{b}_1 = [\cos(\theta), -\sin(\theta)]$, $\vec{b}_2 = [-\cos(\theta), \sin(\theta)]$, $\vec{b}_3 = (1,0)$, and $\vec{b}_4 = (-1,0)$, in which θ is twist angle. The complex refractive index in an atomic EIT configuration is expressed as $n = \sqrt{1+\chi/2} \approx 1+\chi/2$, where χ is the susceptibility for describing the optical response of the signal field. The susceptibility of four-level *N*-type atomic systems is proportional to the atomic density *N* and the density-matrix element ρ_{31} for the transition $|1\rangle \rightarrow |3\rangle$. The density-matrix equations for the four-level *N*-type atomic system under the rotating-wave approximation are given by [1]

$$
\begin{aligned}
\dot{\rho}_{22} &= \Gamma_{42}\rho_{44} + \Gamma_{32}\rho_{33} - \Gamma_{21}\rho_{22} + \frac{i}{2}(\rho_{32} - \rho_{23})\tilde{\Omega}_c \\
\dot{\rho}_{33} &= \Gamma_{43}\rho_{44} - \Gamma_{32}\rho_{33} - \Gamma_{31}\rho_{33} + \frac{i}{2}\left[(\rho_{23} - \rho_{32})\tilde{\Omega}_c + (\rho_{13} - \rho_{31})\Omega_s\right] \\
\dot{\rho}_{44} &= -\left(\Gamma_{43} + \Gamma_{42} + \Gamma_{41}\right)\rho_{44} + \frac{i}{2}(\rho_{14} - \rho_{41})\tilde{\Omega}_p \\
\dot{\rho}_{21} &= -\tilde{\gamma}_{21}\rho_{21} + \frac{i}{2}(\rho_{31}\tilde{\Omega}_c - \rho_{24}\tilde{\Omega}_p - \rho_{23}\Omega_s) \\
\dot{\rho}_{31} &= -\tilde{\gamma}_{31}\rho_{31} + \frac{i}{2}[\rho_{21}\tilde{\Omega}_c - \rho_{34}\tilde{\Omega}_p + (\rho_{11} - \rho_{33})\Omega_s] \\
\dot{\rho}_{41} &= -\tilde{\gamma}_{41}\rho_{41} + \frac{i}{2}[-\rho_{43}\Omega_s + (\rho_{11} - \rho_{44})\tilde{\Omega}_p] \\
\dot{\rho}_{32} &= -\tilde{\gamma}_{32}\rho_{32} + \frac{i}{2}[\rho_{12}\Omega_s + (\rho_{22} - \rho_{33})\tilde{\Omega}_c] \\
\dot{\rho}_{42} &= -\tilde{\gamma}_{42}\rho_{42} + \frac{i}{2}[\rho_{12}\tilde{\Omega}_p - \rho_{43}\tilde{\Omega}_c] \\
\dot{\rho}_{43} &= -\tilde{\gamma}_{43}\rho_{43} + \frac{i}{2}[\rho_{13}\tilde{\Omega}_p - \rho_{42}\tilde{\Omega}_c - \rho_{41}\Omega_s] \\
\rho_{11} + \rho_{22} + \rho_{33} + \rho_{44} &= 1
\end{aligned}
\tag{S3}
$$

Here, Γ_{ij} is the decaying rate between $|i\rangle$ and $|j\rangle$, and $\gamma_{ij} = (\Gamma_i + \Gamma_j)/2$ is the decoherence rate. Among them, $\tilde{\gamma}_{21} = \gamma_{21} - i(\Delta_s - \Delta_c)$, $\tilde{\gamma}_{31} = \gamma_{31} - i\Delta_s$, $\tilde{\gamma}_{41} = \gamma_{41} - i\Delta_p$, $\tilde{\gamma}_{32} = \gamma_{32} - i\Delta_c$, $\tilde{\gamma}_{42} = \gamma_{42} - i(\Delta_c + \Delta_p - \Delta_s)$, $\tilde{\gamma}_{43} = \gamma_{43} - i(\Delta_p - \Delta_s)$, Δ_s, Δ_c, and Δ_p are defined as the frequency detunings of the signal, control and pump fields, respectively. According to the relation $2N\mu_{13}\rho_{31} = \varepsilon_0\chi E_s$, the corresponding susceptibility can be obtained by numerically solving ρ_{31} in Eq. (S3) under steady-state approximation. Since $\Omega_s \ll \Omega_c, \Omega_p$, higher-order terms of Ω_s^2 are ignored in the calculation. Thus, the susceptibility is not affected by Ω_s but is determined by the detuning Δ_s.

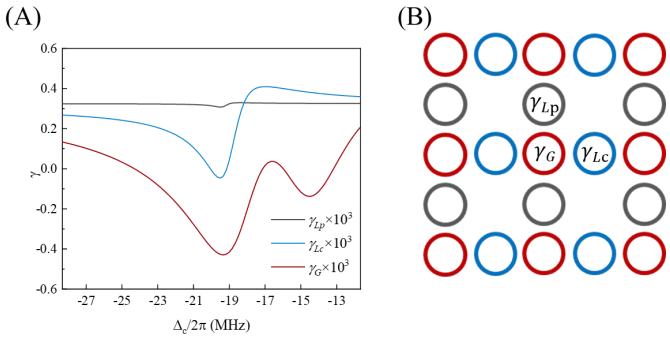

Figure S2. Gain-loss profile in the non-Hermitian twisted photonic lattice. (A) Dependence of the gain (γ_G in red curve) and two types of losses (γ_{Lc} in blue curve and γ_{Lp} in black curve) on Δ_c. (B) Schematic representation of the gain-loss distribution in the non-Hermitian twisted photonic lattice. Black and blue circles denote regions of loss, and red circles denote gain. Other parameters are $\Omega_s = 2\pi \times 4.8$ MHz, $\Omega_p = 2\pi \times 2.5$ MHz, $\Delta_s = -2\pi \times 15$ MHz, $\Delta_p = 2\pi \times 6$ MHz.

The imaginary part of the refractive index (n_I), representing the gain and loss, is shaped by active Raman gain and modified absorption resulting from light amplification and laser-induced atomic coherence [2]. Figure S2(A) plots the calculated n_I at three representative positions: an overlapping region of the two stripe fields (red

curve), a region influenced only by the control beam (blue curve), and a region influenced only by the pump beam (black curve), as a function of Δ_c. Within a specific range of Δ_c, n_I at the overlapping region becomes negative, indicating net gain (γ_G), while the other two regions remain positive, corresponding to absorption losses (γ_{Lp} or γ_{Lc}). As Δ_c is tuned from $-2\pi \times 25$ MHz to $-2\pi \times 20$ MHz, γ_{Lp} remains nearly constant, whereas γ_{Lc} gradually decreases, resulting in an increasing imbalance between the two loss channels. Figure S2(B) provides a schematic representation of the gain-loss distribution in the twisted non-Hermitian lattice [3]. Black and blue circles denote regions dominated by loss, while red circles mark regions exhibiting gain.

S3. Parameter sensitivity of flat band and localization regime

The flat-band and directional-localization regime demonstrated in main text emerges over a finite and continuous detuning window, rather than at a single fine-tuned point. Figure S3 presents a finer detuning interval than that shown in the main text of Figure 2, allowing a more detailed tracking of the flat-band evolution over Δ_c ranging from $-2\pi\times21.5$ MHz to $-2\pi\times18.3$ MHz. As Δ_c increases, the initially overlapping bands near the *M* point gradually develop a local flat band accompanied by an enhanced imaginary component, indicating the strengthening of non-Hermiticity. The flat band becomes most pronounced around $\Delta_c \approx -2\pi\times20$ MHz, where the gain-loss contrast is maximized. With further increase of Δ_c, the non-Hermitian effect weakens and the flat band progressively disappears. These results demonstrate that flat-band formation occurs within a finite and continuous detuning window, rather than at a single fine-tuned point.

Moreover, the flat-band-induced directional localization arises from the competition between gain-loss modulation and inter-channel coupling, rather than requiring an exact gain-loss balance. Despite the inherent disorder of a warm atomic vapor system, including atomic density inhomogeneity, finite laser linewidths, and imperfect lattice contrast, the localization is reproducibly observed across different twist angles and control parameters, demonstrating good tolerance to disorder and experimental nonidealities.

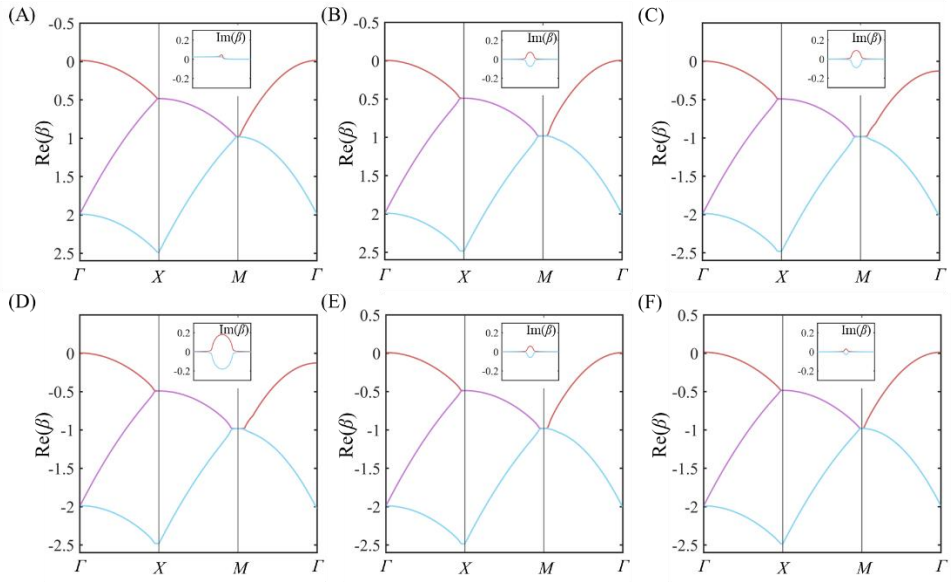

Figure S3. Band structures along the high symmetry lines. The illustrations are corresponding imaginary part of band structures around *M*. Here, $\Delta_c = -2\pi\times21.5$ MHz in (A), $\Delta_c = -2\pi\times21$ MHz in (B), $\Delta_c = -2\pi\times20.5$ MHz in (C), $\Delta_c = -2\pi\times20$ MHz in (D), $\Delta_c = -2\pi\times19$ MHz in (E), and $\Delta_c = -2\pi\times18.3$ MHz in (F). The other parameters are the same as those in Figure 1 of the main text.

S4. Brillouin zone construction and band structure evolution with twist angle

The structure of the twisted photonic lattice at $\theta \neq 90^{\circ}$ is shown in Figure S4. The real-space basis vectors are expressed as $\vec{a}_1 = R\vec{x}$ and $\vec{a}_2 = R\sin(\theta)\vec{x} - R\cos(\theta)\vec{y}$, where θ is the angle between $\vec{a}_1$ and $\vec{a}_2$. By the standard orthogonality condition $(\vec{a}_i \cdot \vec{b}_j = 2\pi\delta_{ij})$, the basis vectors of reciprocal lattice are $\vec{b}_1 = \frac{2\pi}{R\sin(\theta)}\vec{x}$ and $\vec{b}_2 = -\frac{2\pi}{R}\cot(\theta)\vec{x} - \frac{2\pi}{R\sin(\theta)}\vec{y}$. For the twisted photonic lattice, the any reciprocal vector is $\vec{G} = m\vec{b}_1 + m\vec{b}_2$ (m, n is positive integers).

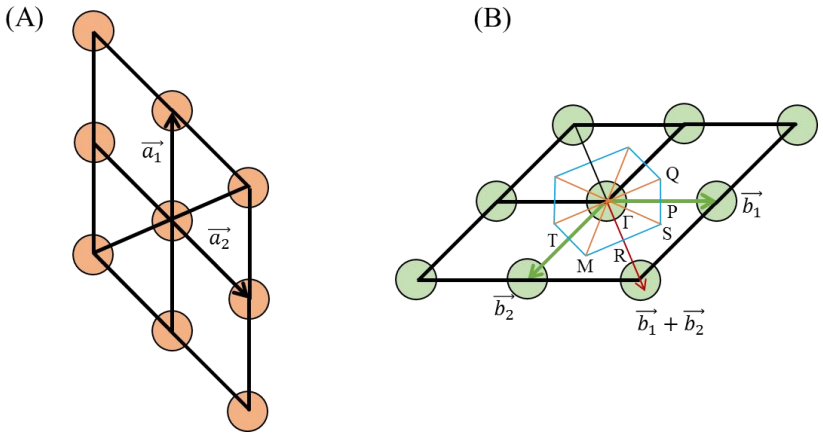

Figure S4. Brillouin zone construction in twisted photonic lattice. (A) The real-space lattice of the twisted photonic lattice. (B) The first Brillouin zone of twisted photonic lattice.

The Brillouin zone is defined as the region enclosed by the perpendicular bisector planes of all reciprocal-lattice vectors emanating from the origin and the smallest such region is the first Brillouin zone. When $\theta < 90^{\circ}$, the first Brillouin zone is hexagonal, and the reciprocal vectors contributing to it are $\pm\vec{b}_1$, $\pm\vec{b}_2$ and $\pm(\vec{b}_1 + \vec{b}_2)$, as shown in Figure S4(B). The high-symmetry points (e.g., *P* and *R*) and the equations of symmetry lines (*SQ* and *SM*) follow directly from the properties of the perpendicular bisectors. Other high-symmetry points are obtained as intersection points of two perpendicular-bisector lines.

Therefore, the *P* and *R* points are located at $(\frac{\pi}{R\sin(\theta)}, 0)$ and $\left[\frac{\pi(1-\cos(\theta))}{R\sin(\theta)}, \frac{\pi}{R}\right]$, and *S*, *Q* and *M* points are $\left[\frac{\pi}{R\sin(\theta)}, \frac{\pi(1-\cos(\theta))}{R\sin^2(\theta)}\right]$, $\left[\frac{\pi}{R\sin(\theta)}, \frac{\pi\cos(\theta)(1-\cos(\theta))}{R\sin^2(\theta)}\right]$, $\left[\frac{2\cos(\theta)}{1+\cos(\theta)} + \frac{\pi}{R[1+\cos(\theta)]}, \frac{\sin(\theta)}{\cos(\theta)}\left(\frac{2\cos(\theta)}{1+\cos(\theta)} + \frac{\pi}{R(1+\cos(\theta))}\right) - \frac{\pi}{R\sin(\theta)\cos(\theta)}\right]$. At $\theta = 90^{\circ}$, the first Brillouin zone is square, and the coordinates high-symmetry points respectively are $(0,0)$, $(0, \frac{2\pi}{R})$, $(\frac{2\pi}{R}, \frac{2\pi}{R})$. Due to the rotational symmetry of the lattice, the derivation and simulation for $\theta > 90^{\circ}$ are analogous to the $\theta < 90^{\circ}$ case.

Figure S5 shows the band-structure evolution and directional localization as θ increases. In Figure S5(A), the band structure (real part) is plotted along the high-symmetry path [$\Gamma \rightarrow P(X) \rightarrow Q(M) \rightarrow \Gamma$] for various θ. For

small twist angles (θ < 10°), the lattice sites are densely packed, resulting in strong inter-site coupling that suppresses directional localization. At θ = 10°, a point degeneracy appears at the high-symmetry point Q. As the twist angle increases, the reciprocal lattice rotates, modifying the coupling pathways between sites and giving rise to local flat-band features in momentum space. The band structure near point Q evolves from a point degeneracy into a local flat band [4], whose width gradually increases with θ. This trend indicates that directional localization becomes more pronounced at larger twist angles, with the strongest localization observed at θ = 90°, as illustrated in Figs. S5(B) and (C). This geometric control enables dynamic steering of the localization axis in momentum space without modifying the underlying gain-loss balance. The observed momentum-space directional localization is directly linked to the reciprocal lattice of the twisted photonic lattice, whereas non-Hermiticity controls the degree of localization.

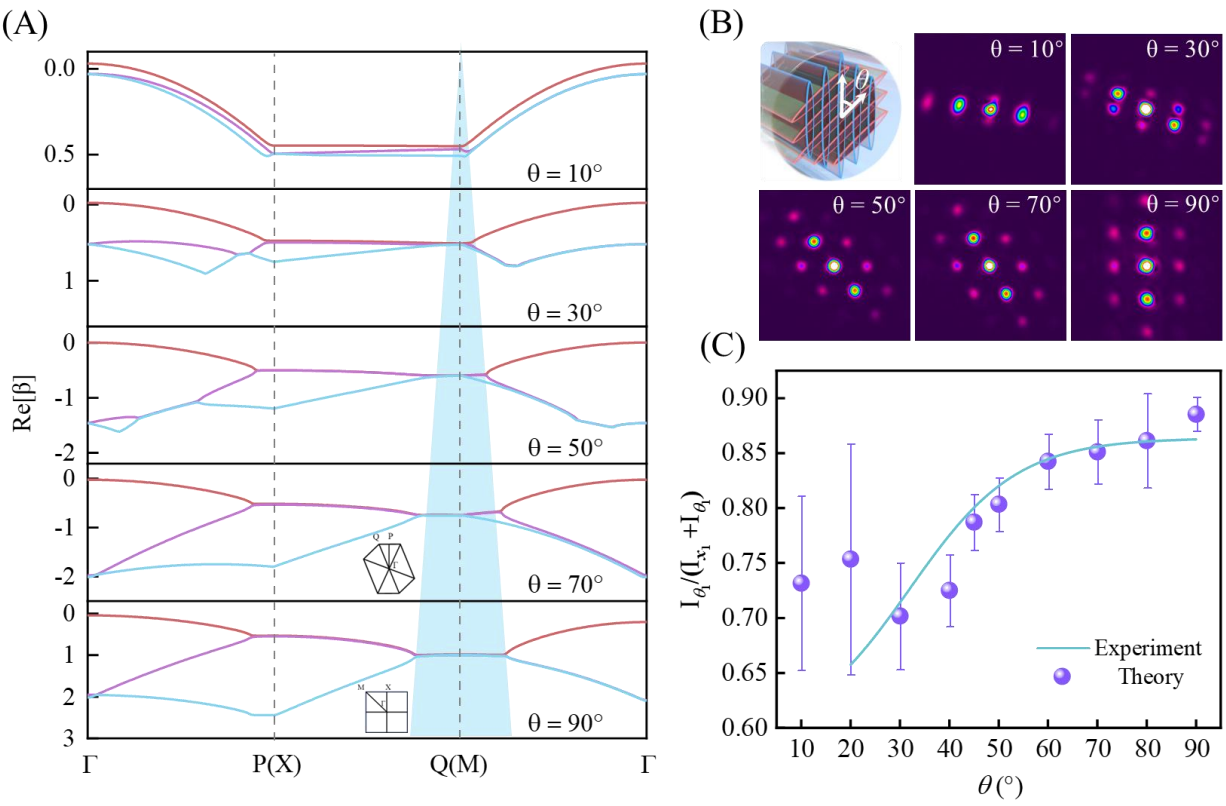

Figure S5. Band structure and directional localization factor evolution with twist angle. (A) The real part of band structures along the high symmetry lines with different θ. (B) Momentum-space images with different θ. (C) Measured (purple dots) directional localization factor and theoretical fitting curve as a function of θ. Here, the theoretical parameters are Δ_s = -2π×15 MHz, Δ_c = -2π×20 MHz, Δ_p = 2π×6 MHz, Ω_c = 2π×4.8 MHz, Ω_p = 2π×2.5 MHz, respectively.

S5. Momentum-space imaging under different twist angles and power tuning

Figure S6 provides the full set of the momentum-space images as Δ_c varies for different θ, corresponding to Figure 5(D) in the main text, and exhibiting evolution trends similar to those observed at θ = 90° (Figure 4 in the main text). In each case, the angle between the x-axis and the localization-axis matches the imposed twist angle θ, confirming that the localization direction follows the lattice rotation. The directional localization factor

(DLF) calculated at θ = 120° and 135° show trends essentially similar to those at θ = 60° and 45°. For clarity, these two cases are not included in Figure 5(D) of the main text.

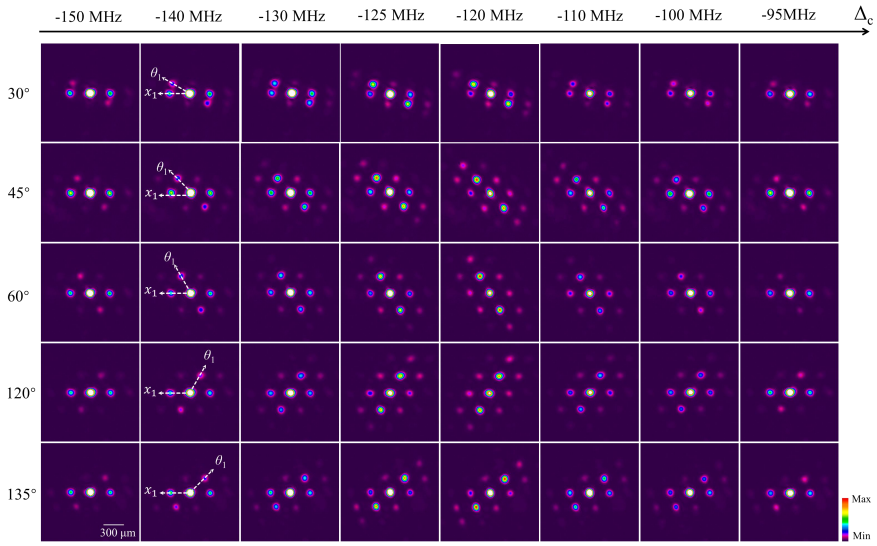

Figure S6. Momentum-space images in different θ with different Δ_c. Here, the experiment parameters are Δ_s = -90 MHz, Δ_c = -120 MHz, Δ_p = 40 MHz, P_c = 45 mW, P_p = 25 mW, and P_s = 5 mW, respectively.

Figure S7 provides the full set of the momentum-space images as control-beam power P_c varies for different θ, corresponding to Figure 6(B) in the main text. As P_c increases, the intensity distribution gradually shifts from the x-axis toward the localization-axis and ultimately becomes strongly confined along this axis [5]. This behavior confirms that higher control-beam power enhances non-Hermitian-induced directional localization. The DLF calculated at θ = 120°, 135° and 150° show trends essentially similar to those at θ = 60°, 45°and 30°. For clarity, these two cases are not included in Figure 6 of the main text.

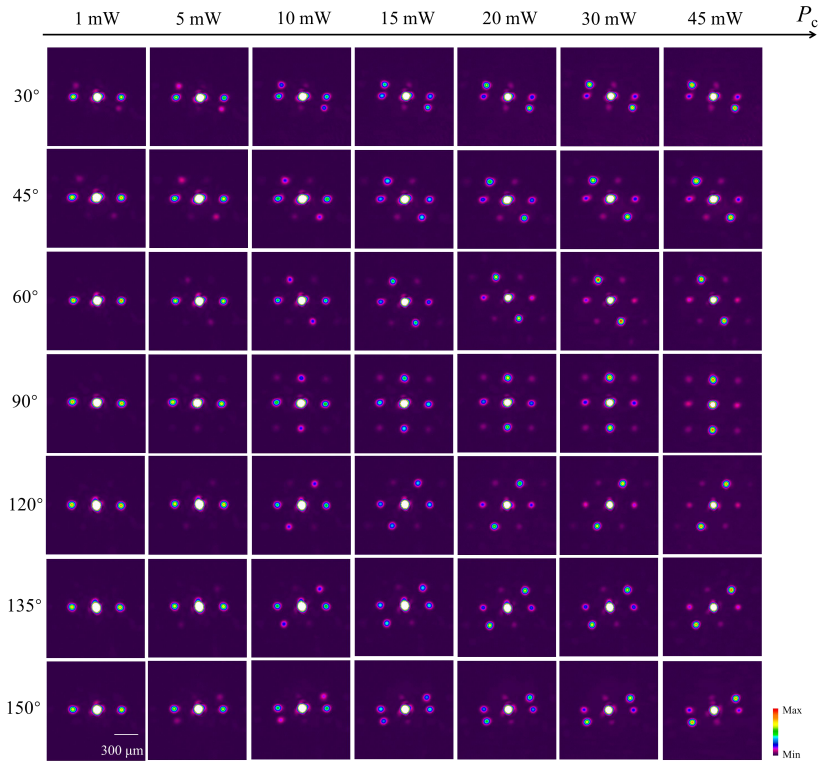

Figure S7. Momentum-space images in different θ with different control beam powers. The other experimental parameters are same as Figure S6.

S6. Real-space imaging under different control-beam detuning and twist angles

Momentum-space changes in the signal-beam images inevitably lead to corresponding changes in its real-space distribution. Figure S8 shows paired momentum- and real-space images for different values of Δ_c. When the momentum-space pattern does not exhibit directional localization (DLF $\leq$ 0.5), the corresponding real-space output remains relatively isotropic, with well-resolved lattice contrast along both transverse directions. In contrast, when the momentum-space distribution exhibit directional localization (Δ_c = -120 MHz), the real-space pattern becomes strongly anisotropic, exhibiting a pronounced stripe-like intensity distribution aligned with the localization direction, while the lattice contrast along the *x* direction is significantly reduced—providing a direct real-space manifestation of channel-selective propagation.

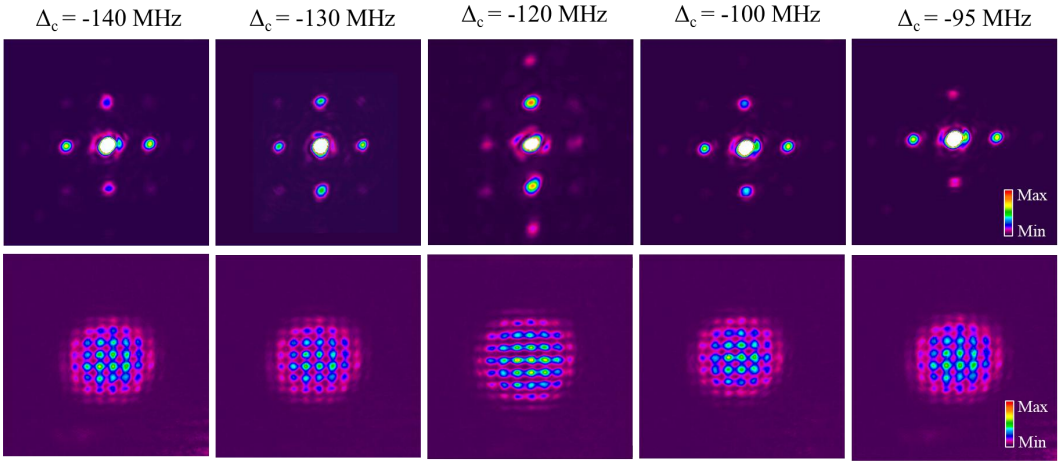

Figure S8. Momentum-space and real-space images with different Δ_c. The other experimental parameters are same as Figure S6.

Furthermore, Figure S9 presents paired momentum- and real-space images for different twist angles θ. As θ is varied, the real-space propagation clearly shows that the selected transport channel rotates synchronously with θ, in direct correspondence with the rotation of the localization-axis observed in momentum space. Together, these observations establish a clear and intuitive correspondence between momentum-space directional localization and channel-selective transport in real space.

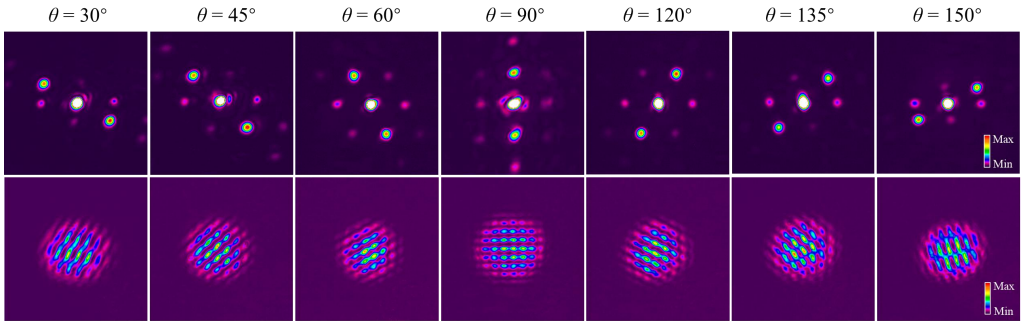

Figure S9. Momentum-space and real-space images with different θ. Here, the experiment parameters are Δ_c = -120 MHz. The other experimental parameters are same as Figure S6.

S7. Momentum-space imaging under different pump-beam intensities

In contrast to the control beam, which provides an efficient knob for tuning the DLF, the pump beam plays a fundamentally different role in our system. Figures S10 (A-B) show the momentum-space images and the extracted DLF for different twist angles θ as a function of the pump-beam power P_p. As P_p increases, the energy distribution in the momentum space remains localized along the localization-axis, and the DLF shows only slight variation, consistently approaches 1.

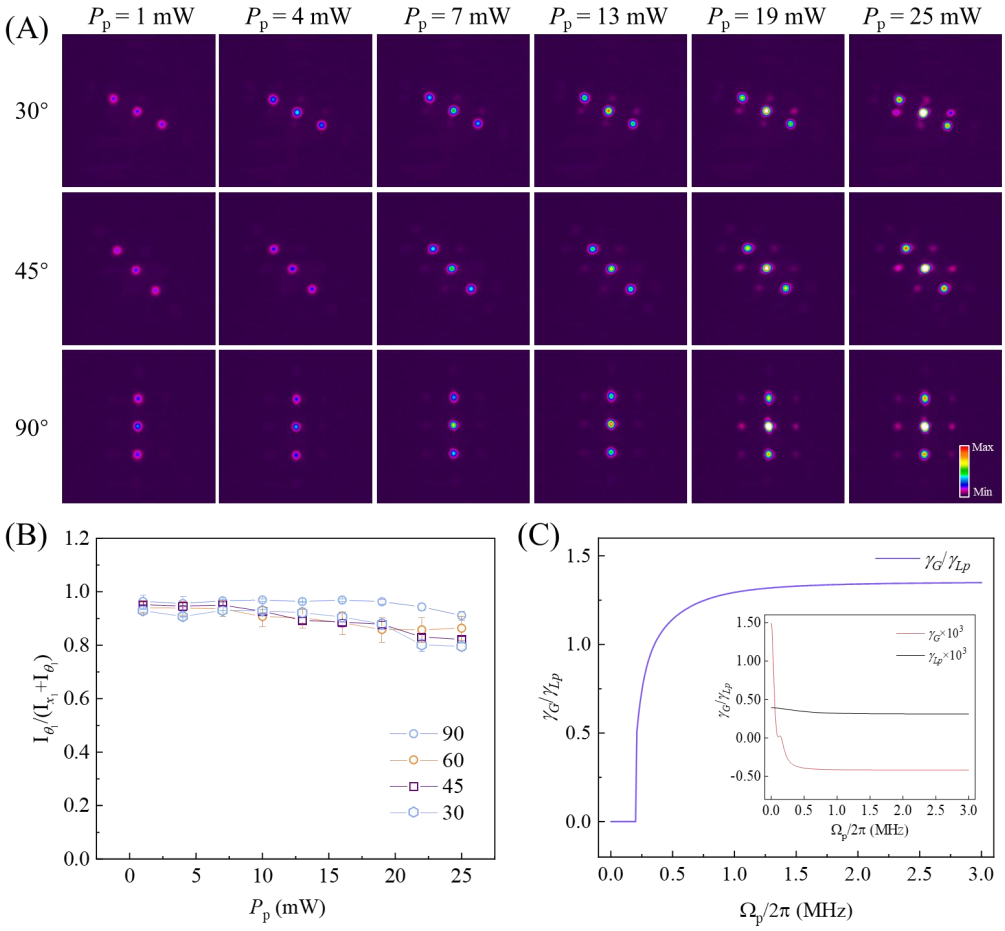

Figure S10. (A)Momentum-space images recorded at different pump beam powers for θ = 30°, 45° and 90°, respectively. (B) Evolution of the directional localization factor as a function of pump beam power for θ = 30°, 45°, 60° and 90°, respectively. Here, Δ_c = -120 MHz. The other experimental parameters are same as Figure S6. (C) Theoretically simulated gain-to-loss ratio (γ_G/γ_{Lp}) as a function of Ω_p, where the inset shows the corresponding variations of the gain (γ_G, red curve) and loss (γ_{Lp}, black curve) with Ω_p. The other theoretical parameters are same as Figure S5.

To qualitatively analyze this behavior, we theoretically simulate the evolution of the gain-loss ratio (γ_G/γ_{Lp}) as a function of the pump Rabi frequency Ω_p, as shown in Figure S10(C). When Ω_p increases from 0 to 0.25×2π MHz, the gain coefficient satisfies $\gamma_G > 0$, indicating that no optical gain is introduced in this regime and the gain-loss ratio remains zero ($\gamma_G/\gamma_{Lp} = 0$), corresponding to $P_p < 7$ mW in the experiment, as shown in Figure S10(A). In this case, the system is mainly governed by an effective three-level V-type configuration, where the contribution of the control field is relatively weak, and the momentum-space field distribution appears localized along the localization axis.

As Ω_p increases further, the Raman gain rises rapidly within a narrow parameter range, causing γ_G/γ_{Lp} to increase sharply and reach values of approximately 1.3. This regime corresponds to pump powers $P_p > 7$ mW, where the experimental results still exhibit localization along the same localization axis, as shown in Figure S10(A). Therefore, although the momentum-space distribution remains localized along the localization axis with increasing pump power, the underlying physical mechanism of this directional localization is fundamentally different from the control field.

Reference

1.Sheng J, Miri MA, Christodoulides DN, Xiao M. PT-symmetric optical potentials in a coherent atomic medium. Physical Review A. 2013;88:041803. [DOI:10.1103/PhysRevA.88.041803]

2.Kang H, Wen L, Zhu Y. Normal or anomalous dispersion and gain in a resonant coherent medium. Physical Review A. 2003;68:063806. [DOI:10.1103/PhysRevA.68.063806]

3.Zhang Z, Feng Y, Ning S, Malpuech G, Solnyshkov DD, Xu Z, et al. Imaging lattice switching with Talbot effect in reconfigurable non-Hermitian photonic graphene. Photonics Research. 2022;10:958. [DOI:10.1364/prj.447404]

4.Wang P, Zheng Y, Chen X, Huang C, Kartashov YV, Torner L, et al. Localization and delocalization of light in photonic moiré lattices. Nature. 2020;577:42-46. [DOI:10.1038/s41586-019-1851-6]

5.Zhang Z, Liang S, Septembre I, Yu J, Huang Y, Liu M, et al. Non-Hermitian delocalization in a two-dimensional photonic quasicrystal. Physical Review Letters. 2024;132:263801. [DOI:10.1103/PhysRevLett.132.263801]